This is a preprint, the final version is subject to change, of the American Mineralogist (MSA)
Cite as Authors (Year) Title. American Mineralogist, in press.
(DOI will not work until issue is live.) DOI: http://dx.doi.org/10.2138/am-2016-5820

Revision 1 of manuscript #5820

Influence of the octahedral cationic-site occupancies on the framework vibrations of Li-free tourmalines

Anke Watenphul[1*], Jochen Schlüter[2], Ferdinando Bosi[3], Henrik Skogby[4], Thomas Malcherek[1], and Boriana Mihailova[1]

[1]Fachbereich Geowissenschaften, Universität Hamburg, Grindelallee 48, D-20146 Hamburg, Germany

[2]Centrum für Naturkunde, Mineralogisches Museum, Universität Hamburg, Grindelallee 48, D-20146 Hamburg

[3]Dipartimento die Scienze della Terra, Sapienza Università di Roma, Piazzale Aldo Moro 5, I-00185 Rome, Italy

[4]Department of Geosciences, Swedish Museum of Natural History, Box 50007, SE-10405 Stockholm, Sweden

[*]corresponding author: anke.watenphul@uni-hamburg.de

This is a preprint, the final version is subject to change, of the American Mineralogist (MSA)
Cite as Authors (Year) Title. American Mineralogist, in press.
(DOI will not work until issue is live.) DOI: http://dx.doi.org/10.2138/am-2016-5820

ABSTRACT

Tourmalines, $XY_3Z_6T_6O_{18}(BO_3)_3V_3W$, are excellent petrogenetic indicators as they capture the signature of the host rock bulk composition. Raman spectra of tourmalines can be used as fingerprints for species identification and crystal chemical analysis. While Li-bearing species are directly distinguishable by the shape of the OH-stretching vibrations, the discrimination of Mg- and Fe-dominant species can be hindered by the coexistence of at least 2 types of octahedrally coordinated R^{n+} cations.

Thirty Li-free tourmaline samples comprising fourteen different species were studied by Raman spectroscopy and electron microprobe. All nine Fe^{3+}-bearing samples were analyzed also by single-crystal X-ray diffraction and Mössbauer spectroscopy. The Raman scattering analysis shows that Mg-dominant species can be immediately distinguished from Fe-dominant species by the shape of the vibrational modes at ~200-240 cm^{-1} arising from the YO_6 vibrations. Trivalent Fe can be observed and quantified by shifts of the framework vibrations towards lower wavenumbers. The position of the main ZO_6 vibrational mode (275-375 cm^{-1}) can be used to determine the $^{Z}Fe^{3+}$ content, while the $^{Y}Fe^{3+}$ content can be inferred from the position of the peak at ~315 cm^{-1}. Fits to the data points indicate that the homovalent substitution of Fe^{3+} for Al^{3+} leads to a considerably larger downward shift of the ZO_6 vibrational mode than the heterovalent substitution Mg^{2+} for Al^{3+}. The intensity ratio of the two major YO_6 vibrational modes (200-240 cm^{-1}) of the fully characterized Fe^{3+}-bearing samples reflects the amount of Y-site Mg and thus can be used to deduce the site-occupancy disorder of Mg over the Y and Z site for tourmaline species with Mg ≤ 2 apfu.

By combining the information from framework and OH-stretching vibrations, Raman spectroscopy alone can be used as a, micrometer-scale sensitive non-destructive method for the analysis of tourmaline crystal chemistry including trivalent Fe, which is the major tracer for oxygen fugacity and central for intersite geothermometry.

Keywords: tourmaline, Raman spectroscopy, framework vibrations, trivalent iron

INTRODUCTION

Tourmaline supergroup minerals are common cyclosilicates that occur in a wide range of igneous, metamorphic, and sedimentary environments (e.g., van Hinsberg et al. 2011 and references therein). Being very useful petrogenetic indicators, the complex crystal chemistry of tourmalines has been extensively studied (e.g., Grice et al.1993; Hawthorne et al. 1993; Hawthorne 2002; Pieczka and Kraczka 2004; Bosi and Lucchesi 2007; Henry and Dutrow, 2011; Bosi 2011; Bosi et al. 2015a,b). The generalized formula can be expressed as $XY_3Z_6(T_6O_{18})(BO_3)_3V_3W$ with X = Na^+, Ca^{2+}, □ (= vacancy), K^+; Y = Fe^{2+}, Mg^{2+}, Mn^{2+}, Al^{3+}, Li^+, Fe^{3+}, Cr^{3+}, Ti^{4+}, Zn^{2+}, Cu^{2+}, V^{3+}; Z = Al^{3+}, Fe^{3+}, Mg^{2+}, Fe^{2+}, Cr^{3+}, V^{3+}; T = Si^{4+}, Al^{3+}, B^{3+}; B = B^{3+}; V = $(OH)^-$, O^{2-}; and W = F^-, $(OH)^-$, O^{2-} being the most common cations and anions at each site (Henry et al. 2011). The crystal structure has *R*3*m* space group symmetry and consists of puckered 6-membered rings of corner-sharing TO_4 tetrahedra as well as of units of edge-sharing YO_6 and ZO_6 octahedra further connected by isolated BO_3 triangles (see Fig.1). The X-site cations and W-site anions are located on the three-fold axis of symmetry, on both sides of the ring plane. The W-site anions are shared between three YO_6 octahedra, whereas the V-site anions are shared between one YO_6 and two ZO_6 octahedra (see Fig.1).

The flexibility of the crystal structure is demonstrated by the occurrence of a large variety of possible major, minor, and trace elements occupying the different crystallographic sites. This has the following implications: (1) the tourmaline supergroup currently consists of thirty-four species approved by the International Mineralogical Association (IMA); (2) solid solutions between different end members are common, including dravite–schorl, schorl–elbaite, dravite–uvite, fluor-buergerite–schorl, povondraite–bosiite–oxy-dravite–dravite (e.g., Donney and Barton 1972; Bloodaxe et al. 1999; Žáček et al. 2000; Bosi et al. 2005; Ertl et al. 2016); and (3) there exists occupancy disorder between the Y and Z sites, i.e., elements are distributed across both sites regardless of the ordered end-member formula. The Y-Z occupancy disorder occurs to release short- and long-range structural strains and it is very typical of Mg-Al as well as of Fe^{3+}-Al pairs and to a considerably lesser extent of Fe^{2+}-Al pairs (e.g., Hawthorne 1996; Bosi et al. 2010). Thus the identification of tourmaline species requires not only knowledge of the major-element contents, but also of the valence states of certain cations (Fe, Mn) and their site occupancies. While the chemical composition is usually determined by electron microprobe analysis, commonly under the assumption of a stoichiometric boron content (B = 3 apfu) and fully occupied anionic sites (V+W = 4), the valence state of Fe can be most precisely analyzed by Mössbauer spectroscopy, and site occupancies can be refined from single-crystal X-ray diffraction data. All of these

techniques require different sample preparations and high analytical expenses. Hence, it would be beneficial to gather all the information by a single non-destructive, easy-to-perform analytical technique.

The advantages of Raman spectroscopy for studying the crystal chemistry of complex silicates have been demonstrated among others for feldspars (Mernagh 1991), garnets (Hofmeister and Chopelas 1991), pyroxenes (Wang et al. 2001), amphiboles (Leißner et al. 2015), and tourmalines (Watenphul et al. 2016). In the case of tourmalines, several studies suggest to use the spectral region of the framework vibrations (Alvarez and Coy-Yll 1977; Gasharova et al. 1997; McKeown 2008; Hoang et al. 2011) as well as of the OH-stretching vibrations as fingerprints for the discrimination of different tourmaline species (Fantini et al. 2014; Berryman et al. 2015; Watenphul et al. 2016). In particular Li-rich tourmalines such as elbaite or fluor-liddicoatite can be immediately distinguished from Mg- and Fe-dominant species, e.g., dravite and schorl, by the shape of the OH-stretching modes (Fantini et al. 2014; Watenphul et al. 2016). The shape of the OH-stretching Raman scattering is also quite efficient to discriminate X-site vacant $^{Y}(R^{2+},R^{3+})$-dominant species from the corresponding alkali and calcic species, e.g., foitite vs. schorl (Watenphul et al. 2016) or magnesio-foitite vs. dravite and uvite (Berryman et al. 2015). Alkali/calcic Fe- or Mg-dominant tourmaline species exhibit OH-stretching Raman scattering of similar shape (see Fig.2), but their crystal chemistry can still be determined by the ^{V}OH-stretching peak positions and relative intensities if only one type of impurity element at the Y site is present (Watenphul et al. 2016). However, if there are at least two extra types of octahedrally coordinated R^{n+} cations coexisting along with the end-member Y-site element, the species identification based only on the shape and position of the OH-stretching vibrations can be rather ambiguous. This is due to the inverse correlation between the OH-stretching wavenumber and the average charge of the octahedrally coordinated cations that coordinate the OH group (Gonzalez-Carreño et al. 1988; Martìnez-Alonso et al. 2002). Similar behavior is also known for other hydrous minerals, e.g., amphiboles, micas, and staurolite (Leißner et al. 2015; Robert et al. 1989; Koch-Müller et al. 1997). For example, additional non-negligible amounts of octahedrally coordinated Al and/or Fe^{3+}, i.e., larger than 0.1 atoms per formula unit (apfu), shifts the ^{V}OH-vibrational modes toward lower wavenumbers, whereas the presence of extra Mg and Li leads to a peak shift toward higher wavenumbers. Therefore, the corresponding effects may compensate each other in the case of tourmaline samples with coexisting heterovalent substitution elements on the octahedrally coordinated sites.

The aim of this study is to analyze in detail the Raman scattering generated by the framework vibrations of various, mostly Li-free, natural tourmaline species, focusing on the vibrational modes of the YO_6 and ZO_6

107 octahedra. Special emphasis is thereby placed on Fe^{3+}-containing samples as an easy and reliable identification
108 of Fe^{3+} allows for important inferences on the host rock compositions. The Raman spectroscopic results on the
109 Y- and Z-site occupancies are correlated with data from complementary electron microprobe analysis, single-
110 crystal X-ray diffraction, and Mössbauer spectroscopy to establish a more reliable approach for non-destructive
111 tourmaline species identification and crystal-chemistry analysis, combining the information from the Raman
112 spectra of framework and OH-stretching vibrations.
113
114 ## MATERIALS AND METHODS
115
116 ### Samples
117 Thirty natural tourmaline samples from worldwide localities are examined in this study. Table 1 gives
118 the structural formulae and references to previous studies, when applicable. Sample S59 (H-rich "buergerite")
119 was annealed for 110 h at 700 °C and sample S51 (oxy-dravite) was kept at 800 °C for 20 h to oxidize Fe^{2+} to
120 Fe^{3+} as described by Filip et al. (2012). Sample S57 was analyzed by single-crystal X-ray diffraction, electron
121 microprobe (WDS mode) and optical absorption spectroscopy in order to determine the site populations and the
122 Fe^{2+}/Fe^{3+} and Mn^{2+}/Mn^{3+} ratio (work in progress).
123
124 ### Raman spectroscopy
125 Raman scattering experiments were conducted in backscattering geometry with a Horiba Jobin-Yvon
126 T64000 triple-monochromator spectrometer (holographic gratings of 1800 grooves/mm) equipped with an
127 Olympus BX41 confocal microscope (Olympus LM Plan FLN 50x objective with a numerical aperture of 0.5)
128 and a Symphony liquid-N_2-cooled charge-coupled device detector. Raman spectra of all samples were excited
129 either by the 488.0 or 514.5-nm line of a Coherent 90C Fred Ar^+ laser. For both laser lines the laser power on the
130 sample surface was approximately 14 mW to ensure no sample overheating during the experiment. The achieved
131 spectral resolution was ~2 cm^{-1} and the accuracy in determining the peak positions was ~0.35 cm^{-1}. The
132 spectrometer was calibrated to the silicon Raman peak at 520.5 cm^{-1}. Further experimental and analytical details
133 are given by Watenphul et al. (2016).
134 Polarized Raman spectra in $\bar{y}(zz)y$ scattering geometry (Porto's notation; Porto and Scott 1967) were
135 collected for all samples in the spectral range 15-4000 cm^{-1}. The acquisition time was chosen to yield a

satisfactory signal-to-noise ratio, thus most spectra were collected for 20 s averaging over 10 accumulations. The OriginPro® 9.1 software package was used for data evaluation. The collected spectra were baseline corrected for the continuum luminescence background when necessary, temperature-reduced to account for the Bose-Einstein occupation factor (Kuzmany 2009), and normalized to the acquisition time. Peak positions, full widths at half maximum (FWHMs), and integrated intensities were determined from fits with pseudo-Voigt functions ($PV = (1-q) * Lorentz + q * Gauss$, q is the weight coefficient). The criterion for the maximum number of fitted peaks was $\Delta I < I/2$, where I and ΔI are the calculated magnitude and uncertainty of each peak intensity, respectively.

Electron microprobe analysis (EMPA)

Chemical analyses of polished specimens of the samples first studied here were obtained using a Cameca SX-100 SEM system with a wavelength-dispersive detector. The energy of the electron beam was 15 keV and the beam current was 20 nA. The following standards were used: LiF for F, albite for Na, MgO for Mg, Al_2O_3 for Al, andradite for Si, Ca, and Fe, vanadinite for Cl and V, orthoclase for K, $MnTiO_3$ for Ti and Mn, Cr_2O_3 for Cr, olivenite for Cu, $SrTiO_3$ for Sr, and Ba-glass for Ba. The acquisition times were 20 s for Na, K, Mg, Ca, Mn, Fe, Al, Ti, and Si, 60 s for Ba, Sr, Cu, Cr, and Cl, and 120 s for F. The acquisition time to collect the background level on both sides of the corresponding peak was a half of the peak acquisition time. The program WinTcac (Yavuz et al. 2014) was used to calculate the chemical formulae and also to classify the tourmaline species. The latter was additionally verified by the spreadsheet in the supplement of Henry et al. (2011). About 25 to 50 spot analyses were carried out for each sample to achieve statistical standard deviations allowing for a compositional precision of about 0.02 apfu for each element in the calculated chemical formulas.

RESULTS AND DISCUSSION

Polarized $\bar{y}(zz)y$ Raman spectra of selected tourmaline samples in the spectral region of the framework and OH-stretching vibrations are shown in Figure 2. Four main ranges of framework vibrations are identified that, according to lattice dynamics calculations (Mihailova et al. 1996; McKeown 2008), can be attributed to the following vibrating groups: (i) the range ~200-240 cm^{-1} is dominated by YO_6 vibrations; (ii) the strongest Raman peak that appears in the range ~360-375 cm^{-1} for ^{Z}Al-dominant species is generated by ZO_6 vibrations

and it considerably shifts toward lower wavenumbers (~ 277 cm^{-1}) for $^{Z}Fe^{3+}$-rich species; (iii) the range ~650-720 cm^{-1} is dominated by breathing modes of bridging oxygen atoms of TO_4 rings; and (iv) the range ~960-1120 cm^{-1} arises predominantly from TO_4 stretching modes. Note that the TO_4 ring and stretching vibrations in $^{Z}Fe^{3+}$-rich species also exhibit significant shifts toward lower wavenumbers (~ 450-550 cm^{-1}), which is most probably related to the overall expansion of the unit cell upon the incorporation of Fe^{3+} at the Z site (Grice et al. 1993) and overall weakening of the metal-oxide interactions.

Magnesium- and Fe-dominant tourmalines can be immediately discriminated by the spectral shape of the YO_6 vibrations. All Mg-dominant tourmalines exhibit a clearly resolved peak doublet, labeled as P_1 and P_2 in Fig. 2, with a subtle shoulder at higher phonon energies and an intensity ratio $I_1/I_2 \sim 1$. In contrast, Fe-dominant species show mostly one well-defined peak with sometimes less-resolved shoulders on either side (Fig. 2).

The behavior of the ZO_6 vibration

For all tourmaline species the dominant ZO_6 vibrational mode produces a strong well-resolved Raman peak, which is marked by a line in Figure 2. Therefore, even small shifts in its position due to changes in the crystal chemistry can be experimentally well detected. Figure 3a-c shows the fitted peak position in dependence of the total octahedral contents of ^{Y+Z}Al, $^{Y+Z}(Fe^{2+}+Fe^{3+})$, and ^{Y+Z}Mg for all studied samples. As it can be clearly seen, Mg- and Fe^{2+}-dominant tourmalines are practically indistinguishable by the position of the ZO_6 vibration for all octahedral elements. The small spread in the data of ±6 cm^{-1} (see supplemental table 1) originates most likely from additional minor and trace elements. It should be noted that no influence of the X-site occupancy on the spectra is experimentally observed, although such has been predicted by lattice dynamics calculations (McKeown 2008). Likewise, Y-/Z-site occupancy disorder of Mg and Al typical of dravite, fluor-dravite, oxy-dravite, and uvite (e.g., Hawthorne et al. 1993; Clark et al. 2011; Bosi and Skogby 2013) is difficult to determine from the position of the main ZO_6 vibration, as the spread in the peak positions for Mg-dominant tourmaline species amounts only to ±3.5 cm^{-1}. This indicates that either the degree of Y-/Z-site disorder is similar for all studied samples or that the shift of $\omega(ZO_6)$ due to ^{Z}Mg replacing ^{Z}Al is small and possibly also masked by other factors, i.e. Fe^{3+} and/or trace elements.

Some samples that are rich in Fe^{3+} clearly exhibit a lower wavenumber of the ZO_6 vibration than the rest of the samples. In particular, the position of the dominant ZO_6 vibration of povondraite is shifted by almost a hundred wavenumbers to 277 cm^{-1}. However, the mode can still be identified by being the dominant vibration in

194 the Raman spectrum, although its intensity in comparison with the other modes in this spectral region is lower
195 compared to other tourmaline species shown in Figure 2, which is due to the different dominant element at the Z
196 site, i.e. $^{Z}Fe^{3+}$ instead of $^{Z}Al^{3+}$, and differences in the ratios of the Z-site element contents. To study whether the
197 peak shift is entirely a unit-cell-volume effect or whether it also provides information about the site occupancy,
198 we considered the dependence of $\omega(ZO_6)$ on the content of Y-site Al, Fe^{3+}, and Mg (Figs 3d,e,f) as well as on the
199 content of Z-site Al, Fe^{3+}, and Mg (Figs 3g,h,i) for all Fe^{3+}-containing samples with site occupancies derived
200 from single-crystal X-ray diffraction.

201 As can be expected, no dependence of $\omega(ZO_6)$ at the Y-site contents of Al, Fe^{3+}, and Mg can be
202 observed (Fig. 3d,e,f). In strong contrast, $\omega(ZO_6)$ gradually increases with increasing ^{Z}Al content (Fig. 3g), and
203 decreases with increasing $^{Z}Fe^{3+}$ content (Fig. 3h). $\omega(ZO_6)$ also decreases with increasing ^{Z}Mg content (Fig. 3i),
204 although the data are more dispersed. Fits with 2nd-order polynomial functions indicate that $^{Z}Fe^{3+}$ and ^{Z}Mg are
205 complementary to each other in substituting Al at the Z site, with ^{Z}Mg having a maximum of about 2 apfu and
206 $^{Z}Fe^{3+}$ having a maximum of about 4 apfu. Note that the linear term in the 2nd-order polynomial fits of the $\omega(ZO_6)$
207 vs. 6-^{Z}Al, $\omega(ZO_6)$ vs. $^{Z}Fe^{3+}$ and $\omega(ZO_6)$ vs ^{Z}Mg dataset is zero within the uncertainties. The goodness of fit R^2
208 for $\omega(ZO_6)$ vs. $^{Z}Fe^{3+}$ ($R^2 \sim 0.97$) almost equals that of $\omega(ZO_6)$ vs. ^{Z}Al ($R^2 \sim 0.99$), whereas the data points for
209 $\omega(ZO_6)$ as a function of ^{Z}Mg are significantly more dispersed ($R^2 \sim 0.74$) (Table 2). This indicates that the
210 homovalent Fe^{3+}-Al substitution is the major reason for the downward wavenumber shift of the ZO_6 vibrational
211 mode. However, the minor effect of Mg cannot be entirely neglected although it is difficult to quantify.

212 The dependence of $\omega(ZO_6)$ on 6–^{Z}Al, which gives the content of non-aluminum Z-site cations, allows
213 for the unambiguous determination using the relation, $6 - {}^{Z}\mathrm{Al} = \sqrt{[(371 \pm 1) - \omega(\mathrm{ZO}_6)]/(3.1 \pm 0.1)}$. For
214 samples that contain none or very little $^{Z}Fe^{3+}$, this content typically equals the content of Z-site Mg. The content
215 of Fe^{3+} at the Z site can be reliably determined using the relation ${}^{Z}\mathrm{Fe}^{3+} = \sqrt{[(367 \pm 2) - \omega(\mathrm{ZO}_6)]/(6 \pm 1)}$.
216 Generally, the quantification of ^{Z}Mg and $^{Z}Fe^{3+}$ contents requires to combine the information provided by the OH
217 stretching and the framework vibrations as discussed below for the showcase.

218 In addition to the dependence of the position of the ZO_6 vibration on the octahedrally coordinated metal
219 cation contents there should also be a dependence of the full width at half maximum (FWHM) of this vibration.
220 The analysis of these data indicates similar trends as observed for $\omega(ZO_6)$, but the datasets exhibit larger errors.
221 Besides, the analysis of the FWHMs as well as of the integrated peak intensities strongly depends on the chosen
222 baseline and the weight coefficient *q* determining the ratio of Gaussian and Lorentzian component. The proper

223 determination of the former might be difficult if the sample shows considerable photoluminescence due to high
224 amounts of incorporated trace elements. The latter might vary due to occupancy disorder on the corresponding
225 crystallographic site. Therefore, it is advisable to use the trends in the peak positions rather than the FWHMs.
226
227 **The behavior of the peak P_3 near 315 cm^{-1}**
228 The comparison of the framework vibrational modes of different tourmaline species showed that the
229 vibrational mode, labeled as P_3 in Figure 2, exhibits a shift from ~315 cm^{-1} to ~ 300 cm^{-1} for all $^{Y}Fe^{3+}$-rich
230 samples except for povondraite (see supplemental table 1). The corresponding peak for povondraite appears
231 either at significantly lower wavenumber ~ 230 cm^{-1} due to the large unit-cell volume or it is also near 300 cm^{-1},
232 but it is overlapped by the stronger ZO_6 peaks. Because of the uncertainty in the peak assignment, povondraite
233 will be excluded from this analysis. Lattice dynamics calculations of fluor-buergerite (McKeown 2008) suggest
234 that the Raman peak near 315 cm^{-1} is predominantly associated with bending vibrations of the YO_6 octahedra
235 and secondary contributions from deformation vibrations of the ZO_6 octahedra, external modes of the BO_3 and
236 TO_4 groups, and displacements of X-site cations along the *c* axis. The analysis of the experimental Raman data
237 reveals that there is no detectable influence of the X-site occupancy on the position of P_3. Thus, variations in the
238 position of P_3 can be indeed attributed mainly to changes in the Y-site occupancy.
239 A thorough analysis of the Fe^{3+}-bearing tourmaline samples shows that the position of P_3 linearly
240 decreases with increasing Fe^{3+} content at the Y site (Fig. 4e), whereas there is no clear dependence on ^{Y}Al and
241 ^{Y}Mg, as revealed by the considerably worse goodness of fit R^2 (Fig. 4d, f). The absence of correlated trends of
242 the P_3 peak position with ^{Y}Al and ^{Y}Mg most probably stems from the larger structural flexibility of the Y site as
243 suggested by its larger chemical variability, including minor and trace elements. Nevertheless, the goodness of
244 fit for $^{Y}Fe^{3+}$ clearly shows that the position of P_3 is a good indicator for Fe^{3+} at the Y site and the equation of the
245 fitting can be used for simple determination of the $^{Y}Fe^{3+}$ content.
246
247 **The behavior of the P_1-P_2 doublet**
248 The spectral region of the YO_6 vibration shows multiple, partly overlapping peaks (Fig. 2). For Mg-
249 dominant species there are two very well resolved Raman signals at 215 and 243 cm^{-1}, labeled in Figure 2 as P_1
250 and P_2, while the spectral shape of Fe-dominant species is more complex. If one considers the main peak as P_2
251 and the shoulder on the lower-energy side as P_1, the difference $\Delta\omega = (\omega_2 - \omega_1)$ and the intensity ratio I_1/I_2 can be

252 calculated for all samples. $\Delta\omega$ is about 25-30 cm^{-1} for all Mg-dominant species and decreases significantly to
253 about 10-18 cm^{-1} for the Fe^{2+}-dominant species (see supplemental table 1). There is no distinct trend for the Fe^{3+}-
254 dominant samples. The wavenumber difference $\Delta\omega$ slightly increases with the total Mg content, while there
255 seem to be no dependencies on ^{Y+Z}Al and ^{Y+Z}Fe. A detailed analysis of the dependence of $\Delta\omega$ on the Y-site Mg
256 and Al was not possible due to the absence of enough samples on hand with refined site occupancies. If only the
257 Fe^{3+}-bearing samples previously studied by single-crystal X-ray diffraction are considered, no distinct trends are
258 observed.

259 The intensity ratio I_1/I_2 ranges between 0.7 and 1.3 for the Mg-dominant species. The spread is
260 considerably larger for the Fe^{2+}- and Fe^{3+}-dominant samples spanning almost the complete range between 0 and
261 1. One might assume a linear negative correlation between the content of $^{Y}Fe^{3+}$ and I_1/I_2 (Fig. 5b), but a few data
262 points considerably deviate from this trend and therefore the intensity ratio could be used only as a secondary
263 indicator for the presence of $^{Y}Fe^{3+}$, along with the primary indicator: the wavenumber of peak P_3 ranging from
264 ~315 cm^{-1} to ~300 cm^{-1} with the increase of $^{Y}Fe^{3+}$. There is also no clear dependence on the content of Y-site Al
265 (Fig. 5a). However, there is an apparent stepwise trend between I_1/I_2 and the content of ^{Y}Mg, with an inflection
266 point corresponding to $^{Y}Mg \sim 0.55$ apfu (Fig. 5c). The ^{Y}Mg content vs. I_1/I_2 can be nicely fitted with a growth
267 function, e.g., Boltzmann function of the type
268 $^{Y}Mg = (1.02 \pm 0.05) - (1.02 \pm 0.05) / (1 + \exp[(I_1 / I_2 - (0.55 \pm 0.04)) / (0.10 \pm 0.03)])$ and this
269 dependence can be used to determine Y-site Mg content in tourmaline species with total Mg ≤ 2 apfu. The latter
270 restriction is related to the fact that the data presented in Figure 5b have such compositions. It should be however
271 emphasized that all studied dravitic and uvitic samples exhibit intensity ratio $I_1/I_2 \sim 1$ and therefore the
272 framework vibrations should be analyzed in combination with the OH stretching modes (Watenphul et al. 2016)
273 to obtain quantitative information about the total amount of Mg. The quantitative distinction between ^{Y}Mg and
274 ^{Z}Mg via Raman scattering still remains an open issue for tourmalines with total Mg > 2 apfu.

275 It should be underlined that sample S57 contains a substantial amount of Mn^{3+} (see Table. 1). Our
276 previous studies on amphiboles (Leißner et al. 2015) and tourmalines (Watenphul et al. 2016) indicated that
277 Mn^{2+} can hardly be distinguished from Fe^{2+} by Raman spectroscopy. This is also supported by nearly the same
278 wavenumbers of the ^{W}OH-stretching bands observed in infrared spectra of Fe^{2+}-rich elbaite and tsilaisite samples
279 (Bosi et al. 2012; 2015b). Hence, we considered the amount of (Mn^{3+} + Fe^{3+}) for sample S57 rather than only the
280 amount of Fe^{3+}, and the corresponding data points matched very well the trends shown in Figures 3-5, when only

Mn-free samples are considered. This result indicates that one cannot distinguish Mn^{3+} from Fe^{3+} in tourmalines by Raman spectroscopy. However, from the point of view of oxygen fugacity, only the valence state matters ($Mn^{3+} + Fe^{3+}$ vs. $Mn^{2+} + Fe^{2+}$), i.e. the discrimination of Mn^{3+} from Fe^{3+} is insignificant.

CONCLUSIONS

The study of thirty tourmaline samples encompassing fourteen different species showed that Raman spectroscopy is a suitable tool to analyze the crystal chemistry of tourmaline. Even samples with complex Y- and Z-site chemistry, i.e., with impurity element contents larger than 0.1 apfu, can be clearly identified by combining the information from the framework and OH-stretching vibrations. In particular, the incorporation of Fe^{3+} can be identified by downward shifts of the framework vibrational modes. The trends of the positions of the dominant ZO_6 vibrational mode, the position of the peak P_3 near 315 cm^{-1}, and the intensity ratio of the YO_6 vibrational modes $P_1 \sim 215$ cm^{-1} and $P_2 \sim 243$ cm^{-1} with the content of Fe^{3+} can be used to quantify the contents at the Y and Z sites.

The crystallochemical analysis of an Fe^{3+}-bearing tourmaline sample combining the information from the framework and OH-stretching vibrations is illustrated for sample S50 as a showcase (Fig. 6). Note that the ^{V}OH-stretching modes of this sample, as observed by infrared spectroscopy, have been already assigned to various YZZ-YZZ-YZZ chemical species that contain Mg, Al, and Fe^{3+}, after precisely determining the structural formula by a combination of analytical methods (Bosi et al. 2016b). In the following discussion we are going to try to solve the reverse problem: to identify the tourmaline species and to determine the crystallochemical formula only on the basis of the Raman scattering in the entire spectral range.

First, the inspection of the shape of Raman scattering in the range ~200-240 cm^{-1} consists of a well-resolved P_1-P_2 doublet, i.e., the sample is a Mg-dominant tourmaline species. Further on, the region of the ^{W}OH-stretching vibrations shows four peaks (3776±2 cm^{-1}, 3738±1 cm^{-1}, 3674±6 cm^{-1}, 3642±1 cm^{-1}), which correspond within errors well to that of dravite and uvite (Watenphul et al. 2016).

Second, the range 3300-3615 cm^{-1} reveals three ^{V}OH modes at 3567±1 cm^{-1}, 3529±2 cm^{-1}, and 3480±7 cm^{-1}, which according to Watenphul et al. (2016) are assigned to $3^{Y}Mg^{Z}Al^{Z}Al$, $2^{Y}Mg^{Z}Al^{Z}Al$-$^{Y}Al^{Z}Al^{Z}Al$, and $^{Y}Mg^{Z}Al^{Z}Al$-$2^{Y}Al^{Z}Al^{Z}Al$, correspondingly. The ^{V}OH peak positions are shifted towards lower wavenumbers by 5-16 cm^{-1} compared to dravite (Watenphul et al. 2016), which indicates an additional incorporation of significant amount of trivalent elements such as Fe^{3+} and/or variations in the X-site occupancy. The former should have a

stronger effect than the latter, since in general the H3-X distances in tourmalines are rather large (~ 3.60 Å, Gatta et al. 2014) and hence, the H3-X interactions are weak (Hawthorne 2016) and have only a secondary effect on the ^{V}OH vibrations (Watenphul et al. 2016). However, the ^{V}OH-stretching modes associated with possible additional trivalent elements at the Y or Z sites should overlap with the corresponding modes of dravite so that the additional elements cannot be identified nor quantified. Therefore, there are two effects on the ^{V}OH stretching: an additional type of octahedrally coordinated trivalent cations and X-site vacancy, which cannot be separated from each other. Thus, the X-site content calculated from the equation $x_{(Na+Ca)} = [\omega(^{V}OH) - 3547]/30$ for the $3^{Y}Mg^{Z}Al^{Z}Al$ peak (Watenphul et al. 2016) gives only the X-site occupancy minimum. For sample S50 $\omega(^{V}OH) = 3567$ cm^{-1} and therefore the obtained minimum value of ^{X}(Na+Ca) is 0.67 apfu. Assuming disorder of Mg and Al over the Y and Z sites, the integrated intensities of the ^{V}OH modes (Watenphul et al. 2016) give $^{Y+Z}Mg = 2.34 \pm 0.09$ apfu and $^{Y}Al + {}^{Z}Al = (0.66 \pm 0.06) + 6$ apfu.

Third, the dominant ZO_6 vibration is observed at 368±0.1 cm^{-1}. Thus, the calculated content $^{Z}Fe^{3+} = \sqrt{(367-368)/6}$ amounts to 0 apfu, whereas the content of non-aluminum Z-site cations $6 - {}^{Z}Al = \sqrt{(371-368)/3.1}$ is calculated to 0.98 apfu. Assuming that only Mg and Fe^{3+} can replace Al at the Z site, it follows that $^{Z}Mg = 0.98$ apfu. From the value of $\omega_3 = 312 \pm 0.1$ cm^{-1} the Y-site Fe^{3+} content is calculated to $^{Y}Fe^{3+} = (314 - \omega_3)/7 = 0.29$ apfu and the intensity ratio I_1/I_2 of 1.1 indicates a ^{Y}Mg content of 1.02 apfu. Therefore, the framework vibrations reveal a total amount of Mg equal to 2 apfu, which is slightly lower than that calculated from the ^{V}OH stretching modes. The discrepancy is related to the neglected additional types of cations occurring predominantly at the Y site, whose influence is commonly strong on the OH-stretching vibrations. Then, the Al contents can be calculated as $^{Y}Al = (3 - 1.02{}^{Y}Mg - 0.29{}^{Y}Fe^{3+})$ and $^{Z}Al = (6 - 0.98{}^{Z}Mg - 0{}^{Z}Fe^{3+})$.

Finally, assuming stoichiometric amounts of Si and B, the chemical formula of this tourmaline sample is $^{X}[(Na+Ca)_{0.7}\square_{0.3}]^{Y}(Mg_{1.02}Al_{1.69}Fe^{3+}_{0.29})^{Z}(Al_{5.02}Mg_{0.98})Si_6O_{18}(BO_3)_3(OH)_3(O_{0.7}OH_{0.3})$, which is in a good agreement with $^{X}[(Na+K)_{0.85}\square_{0.15}]^{Y}(Mg_{1.03}Al_{1.34}Fe^{3+}_{0.58}Fe^{2+}_{0.02}Ti_{0.03})^{Z}(Al_{4.95}Mg_{1.03}Fe^{3+}_{0.03})^{T}(Si_{5.98}Al_{0.02})O_{18}(BO_3)_3(OH)_3(O_{0.69}F_{0.24}OH_{0.07})$ calculated from EMPA, single-crystal X-ray diffraction, and Mössbauer spectroscopy (Table 1). The sample can be classified as Fe^{3+}-bearing oxy-dravite. Certainly the use of combined EMPA, single-crystal X-ray diffraction and Mössbauer spectroscopy can provide more precise chemical formula, but the approach presented here demonstrates the ability of Raman spectroscopy to be used as a sole, fast, non-destructive method with micrometer-scale length sensitivity for crystallochemical analyses of tourmalines.

IMPLICATIONS

The complex crystal chemistry and zonation of tourmalines allows for recording the geologic evolution of the host rock environment (e.g., van Hinsberg et al. 2011). Several studies have focused on potential geothermometers based on the Mg-Fe exchange between tourmaline and biotite (e.g., Blamart et al. 1992; Henry and Dutrow 1996). In a more rigorous study, the geothermobarometric potential of tourmaline was explored by studies of element exchange among tourmaline and coexisting minerals in metamorphosed rocks and also through experimental exchange between tourmaline and biotite by van Hinsberg and Schumacher (2009). However, they observed considerable spread in K_D-values versus temperature, which was ascribed to intersite partitioning of elements over the Y and Z sites in tourmaline, and concluded that the promising potential of tourmaline geothermobarometry cannot be fulfilled until effects of intersite partitioning and non-ideal interactions are better understood. The current knowledge regarding intersite partitioning is limited and predominantly based on structure refinement and spectroscopic methods, but indicates substantial intersite partitioning coupled to short-range ordering. Recent findings obtained on Fe^{3+}-bearing oxy-dravite (Bosi et al., 2016b) demonstrate that Fe progressively disorders over the Y and Z sites with increasing temperature, whereas Mg orders at the Y site according to the order-disorder reaction $^{Y}Fe + {}^{Z}Mg \leftrightarrow {}^{Z}Fe + {}^{Y}Mg$. As a consequence, a geothermometer may be developed by thermal calibration of this Mg-Fe order-disorder reaction, and thus providing means for more accurate estimates of formation temperatures. Our findings here show that such order-disorder processes may be studied by Raman spectroscopy, which is a relatively easily applied technique. The incorporation of Fe^{3+} and in some cases Mn^{3+} is also of particular interest as it points to the oxygen activity during the formation. Thus, zoned tourmaline samples with different Fe^{3+}/Fe_{total} ratios provide the information on the oxidation history on the host rocks. The valence state of Fe is most precisely studied by Mössbauer spectroscopy, which however typically requires a relatively large amount of sample for standard spectrometer systems. This study showed that Raman spectroscopy is also a suitable tool to detect Fe^{3+} in tourmaline and study its zonation. By comparison with complementary analyses by electron microprobe, Mössbauer spectroscopy and X-ray diffraction, trends between peak positions and octahedrally coordinated Fe contents have been established and proposed to be used for quantification. Such dependencies of Raman peak positions with Fe^{3+} contents should also exist in other complex hydrous silicates like e.g. amphiboles and layered silicates.

Acknowledgements. Financial support by the Deutsche Forschungsgemeinschaft DFG (MI 1127/7-1 and SCHL 549/6-1) and Sapienza University of Rome (Prog. Università 2015 to F.B.) are gratefully acknowledged. The authors thank P. Stutz for sample preparation, S. Heidrich for conducting electron microprobe analysis, M. Lensing-Burgdorf for parts of the Raman spectroscopic measurements, as well as M. Ciriotti and I. Baksheev for providing sample S57 and the bosiite sample, respectively. We also thank M. Koch-Müller and J. Cempírek for their constructive reviews and G.D. Gatta for the editorial handling of the manuscript.

References

Alvarez M.A., and Coy-Yll, R. (1977) Raman spectra of tourmaline. Spectrochimica Acta, 34A, 899-908.

Berryman E.J., Wunder B., Ertl, A., Koch-Müller, M., Rhede, D., Scheidl, K., Giester, G., and Heinrich, W. (2015) Influence of the X-site composition on tourmaline's crystal structure: investigation of synthetic K-dravite, dravite, oxy-uvite, and magnesio-foitite using SREF and Raman spectroscopy. Physics and Chemistry of Minerals, 43, 83–102.

Blamart, D., Boutaleb, M., Sheppard, S., Marignac, C. and Weisbrod, A. (1992) A comparative thermobarometric (chemical and isotopic) study of a tourmalinized pelite and its Sn-Be vein, Walmès, Morocco. European Journal of Mineralogy, 4, 355–368.

Bloodaxe, E.S., Hughes, J.M., Dyar, M.D., Grew, E.S., and Guidotti, C.V. (1999) Linking structure and chemistry in the schorl-dravite series. American Mineralogist, 84, 922-928.

Bosi, F. (2011) Stereochemical constraints in tourmaline: From a short-range to a long-range structure. Canadian Mineralogist, 49, 17-27.

Bosi, F., and Lucchesi, S. (2007) Crystal chemical relationships in the tourmaline group: structural constraints on chemical variability. American Mineralogist, 92, 1054-1063.

Bosi, F., and Skogby, H. (2013) Oxy-dravite, $Na(Al_2Mg)(Al_5Mg)(Si_6O_{18})(BO_3)_3(OH)_3O$, a new mineral species of the tourmaline supergroup. American Mineralogist, 98, 1442-1448.

Bosi, F., Andreozzi, G.B., Federico, M., Graziani, G., and Lucchesi, S. (2005) Crystal chemistry of the elbaite-schorl series. American Mineralogist, 90, 1784-1792.

Bosi, F., Balić-Žunić, T., and Surour, A.A. (2010) Crystal structure analyses of four tourmaline specimens from the Cleopatra's Mines (Egypt) and Jabal Zalm (Saudi Arabia), and the role of Al in the tourmaline group. American Mineralogist, 95, 510-518.

Bosi, F., Skogby, H., Agrosì, G., and Scandale, E. (2012) Tsilaisite, $NaMn_3Al_6(Si_6O_{18})(BO_3)_3(OH)_3OH$, a new mineral species of the tourmaline supergroup from Grotta d'Oggi, San Pietro in Campo, island of Elba, Italy. American Mineralogist, 97, 989–994.

Bosi, F., Skogby, H., Lazor, P., and Reznitskii, L. (2015a) Atomic arrangements around the O3 site in Al- and Cr-rich oxy-tourmalines: a combined EMP, SREF, FTIR and Raman study. Physics and Chemistry of Minerals, 42, 441-453.

Bosi, F., Andreozzi, G.B., Hålenius, U., and Skogby, H. (2015b) Experimental evidence for partial Fe^{2+} disorder at the *Y* and *Z* sites of tourmaline: a combined EMP, SREF, MS, IR and OAS study of schorl. Mineralogical Magazine, 79, 515-528.

Bosi, F., Skogby, H., Ciriotti, M.E., Gadas, P., Novák, M., Cempírek, J., Všianský, D., and Filip, J. (2016a) Lucchesiite, $CaFe^{2+}_3Al_6(Si_6O_{18})(BO_3)_3(OH)_3O$, a new mineral species of the tourmaline supergroup. Mineralogical Magazine, doi 10.1180/minmag.2016.080.067.

Bosi, F., Skogby, H., and Hålenius, U. (2016b) Thermally induced cation redistribution in Fe-bearing oxy-dravite and potential geothermometric implications. Contributions to Mineralogy and Petrology, 171, 47.

Bröcker, M. and Franz, L. (2000) The contact aureole on Tinos (Cyclades, Greece): Tourmaline-biotite geothermometry and Rb-Sr geochronology. Mineralogy and Petrology, 70, 257–283.

Chang, I.F., and Mitra, S.S. (1971) Long wavelength optical phonons in mixed crystals. Advances in Physics, 20, 359-404.

Clark, C.M., Hawthorne, F.C., and Ottolini, L. (2011) Fluor-dravite, $NaMg_3Al_6Si_6O_{18}(BO_3)_3(OH)_3F$, a new mineral species of the tourmaline group from the Crabtree emerald mine, Mitchell County, North Carolina: description and crystal structure. Canadian Mineralogist, 49, 57-62.

Donney, G., and Barton Jr., R. (1972) Refinement of the crystal structure of elbaite and the mechanism of tourmaline solid solution. TMPM Tschermaks Mineralogisch-Petrologische Mitteilungen , 18, 273-286.

Ertl, A., Hughes, J.M., Prowatke, S., Ludwig, T., Prasad, P.S.R., Brandstaetter, F., Koerner, W., Schuster, R., Pertlik, F., and Marschall, H. (2006) Tetrahedrally coordinated boron in tourmalines from the liddicoatite-elbaite series from Madagascar: structure, chemistry and infrared spectroscopic studies. American Mineralogist, 91, 1847-1856.

Ertl, A., Baksheev, I.A., and Giester, G. (2015) Bosiite, a new mineral of the tourmaline supergroup. Periodico di Mineralogia, ECMS 2015, 69-70.

Ertl, A., Baksheev, I.A., and Giester, G. (2016) Bosiite, $NaFe^{3+}_3(Al_4Mg_2)(Si_6O_{18})(BO_3)_3(OH)_3O$, a new ferric member of the tourmaline supergroup from the Darasun gold deposit, Transbaikalia, Russia. European Journal of Mineralogy, 28: doi 10.1127/ejm/2016/0028-2540.

Fantini, C., Tavares, M.C., Krambrock, K., Moreira, R.L., and Righi, A. (2014) Raman and infrared study of hydroxyl sites in natural uvite, fluor-uvite, magnesio-foitite, dravite and elbaite tourmalines. Physics and Chemistry of Minerals, 41, 247-254.

Filip, J., Bosi, F., Novák, M., Skogby, H., Tuček, J., Čuda, J., and Wildner, M. (2012) Iron redox reactions in the tourmaline structure: High-temperature treatment of Fe^{3+}-rich schorl. Geochimica et Cosmochimica Acta, 86, 239-256.

Gasharova, B., Mihailova, B., and Konstantinov, L (1997) Raman spectra of various types of tourmaline. European Journal of Mineralogy, 9, 935-940.

Gatta, G.D., Bosi, F., McIntyre, G.J., and Skogby, H. (2014) First accurate location of two proton sites in tourmaline: a single-crystal neutron diffraction study of oxy-dravite. Mineralogical Magazine, 78, 681–692.

Gonzalez-Carreño, T., Fernandez, M., and Sanz, J. (1988) Infrared and electron microprobe analysis in tourmalines. Physics and Chemistry of Minerals, 15, 452-460. Grice, J.D., Ercit, T.S., and Hawthorne, F.C. (1993) Povondraite, a redefinition of the tourmaline ferridravite. American Mineralogist, 78, 433-436.

Hawthorne, F.C. (1996) Structural mechanisms for light-element variations in tourmaline. Canadian Mineralogist, 34, 123-132.

Hawthorne, F.C. (2002) Bond-valence constraints on the chemical composition of tourmaline. Canadian Mineralogist, 40, 789.797.

Hawthorne, F.C. (2016) Short-range atomic arrangements in minerals. I: The minerals of the amphibole, tourmaline and pyroxene supergroups. European Journal of Mineralogy, 28, doi 10.1127/ejm/2016/0028-2538.

Hawthorne, F.C., MacDonald, D.J., and Burns, P.C. (1993) Reassignment of cation site occupancies in tourmaline: Al-Mg disorder in the crystal structure of dravite. American Mineralogist, 78, 265-270.

Henry, D.J., and Dutrow, B.L. (1996) Metamorphic tourmaline and its petrologic applications. In: Grew ES, Anvitz LM (eds) Boron: mineralogy, petrology and geochemistry, reviews in mineralogy and geochemistry, vol. 33, Mineralogical Society of America, Chantilly, Virginia, pp 503–557.

Henry, D.J., and Dutrow, B.L. (2011) The incorporation of fluorine in tourmaline: internal crystallographic controls or external environmental influences? Canadian Mineralogist, 49, 41-56.

Henry, D.J., Novák, M., Hawthorne, F.C., Ertl, A., Dutrow, B.L., Uher, P., and Pezzotta, F. (2011) Nomenclature of the tourmaline-supergroup minerals. American Mineralogist, 96, 895-913.

Hoang, L.H., Hien, N.T.M., Chen, X.B., Minh, N.V., and Yang, I.-S. (2011) Raman spectroscopic study of various types of tourmalines. Journal of Raman Spectroscopy, 42, 1442-1446.

Hofmeister, A.M., and Chopelas A. (1991) Vibrational spectroscopy of end-member silicate garnets. Physics and Chemistry of Minerals, 17, 503-526.

Kuzmany, H. (2009) Solid-state spectroscopy – An introduction, 554p. Springer, Berlin.

Koch-Müller, M., Langer, K., Behrens, H., and Schuck, G. (1997) Crystal chemistry and infrared spectroscopy in the OH-stretching region of synthetic staurolites. European Journal of Mineralogy, 9, 67-82.

Leißner, L., Schlüter, J., Horn, I, and Mihailova, B. (2015) Exploring the potential of Raman spectroscopy for crystallochemical analyses of complex hydrous silicates: I. Amphiboles. American Mineralogist, 100, 2682-2694.

Lussier, A.J., Aguiar, P.M., Michaelis, V.K., Kroeker, S., and Hawthorne, F.C. (2009) The occurrence of tetrahedrally coordinated Al and B in tourmaline: An ^{11}B and ^{27}Al MAS NMR study. American Mineralogist, 94, 785-792.

Martìnez-Alonso, S., Rustad, J.R., Goetz, A.F.H. (2002) Ab initio quantum mechanical modeling of infrared vibrational frequencies of the OH group in dioctahedral phyllosilicates. Part II: main physical factors governing the OH vibration. American Mineralogist, 87, 1224-1234.

McKeown, D.A. (2008) Raman spectroscopy, vibrational analysis, and heating of buergerite tourmaline. Physics and Chemistry of Minerals, 35, 259-270.

Mernagh, T.P. (1991) Use of the laser Raman microprobe for discrimination amongst feldspar minerals. Journal of Raman Spectroscopy, 22, 453-457.

Mihailova, B., Gasharova, B., and Konstantinov, L. (1996) Influence on non-tetrahedral cations in Si–O vibrations in complex silicates. Journal of Raman Spectroscopy, 27, 829-833.

Momma, K., and Izumi, F. (2011) VESTA 3 for three-dimensional visualization of crystal, volumetric and morphology data. Journal of Applied Crystallography, 44, 1272-1276.

Pieczka, A., and Kraczka, J. (2004) Oxidized tourmalines – a combined chemical, XRD and Mössbauer study. European Journal of Mineralogy, 16, 309-321.

Porto, S.P.S. and Scott, J.F. (1967) Raman spectra of $CaWO_4$, $SrWO_4$, $CaMoO_4$, and $SrMoO_4$. Physical Review, 157, 716-717.

Robert, J.-L., Bény, J.-M., Bény, C., and Volfinger, M. (1989) Characterization of lepidolites by Raman and infrared spectrometries. I. Relationships between OH-stretching wavenumbers and composition. Canadian Mineralogist, 27, 225-235.

Skogby, H., Bosi, F., and Lazor, P. (2012) Short-range order in tourmaline: a vibrational spectroscopic approach to elbaite. Physics and Chemistry of Minerals, 39, 811-816.

van Hinsberg, V.J. and Schumacher, J.C. (2009) The geothermobarometric potential of tourmaline, based on experimental and natural data. American Mineralogist, 94, 761–770.

van Hinsberg, V.J., Henry, D.J., and Marschall, H.R. (2011) Tourmaline: An ideal indicator of its host environment. Canadian Mineralogist, 49, 1-16.

Wang, A., Jolliff B.L., Haskin, L.A., Kuebler, K.E., and Viskupic, K.M. (2001) Characterization and comparison of structural and compositional features of planetary quadrilateral pyroxenes by Raman spectroscopy. American Mineralogist, 86, 90-806.

Watenphul, A., Burgdorf, M., Schlüter, J., Horn, I., Malcherek, T., and Mihailova, B. (2016) Exploring the potential of Raman spectroscopy for crystallochemical analyses of complex hydrous silicates: II. Tourmalines. American Mineralogist, 101, 970-985.

Yavuz, F., Karakaya, N., Yıldırım, D.K., Karakaya, M.Ç., and Kumral, M. (2014) A Windows program for calculation and classification of tourmaline-supergroup (IMA-2011). Computers and Geosciences, 63, 70-87.

Žáček, V., Frýda, J., Petrov, A., and Hyršl, J. (2000) Tourmalines of the povondraite – (oxy)dravite series from the cap rock of meta-evaporite in Alto Chapare, Cochabamba, Bolivia. Journal of the Czech Geological Society, 45, 3-12.

511 **Figure captions**

512

513 **Figure 1.** Crystal structure of tourmaline, space group *R*3*m*, with X-site cations shown in yellow, YO_6
514 octrahedra in brown, ZO_6 octrahedra in light blue, TO_4 tetrahedra in dark blue, and BO_3 groups in green. Oxygen
515 atoms are depicted by red balls, hydrogen atoms by pink balls. The structural data were taken from Ertl et al.
516 (2006), the software package VESTA (Momma and Izumi 2011) was used for figure preparation.

517

518 **Figure 2.** Polarized $\bar{y}(zz)y$ Raman spectra of representative tourmaline samples: dravite (S2), uvite (S39), foitite
519 (S45), schorl (S7), Fe^{3+}-rich schorl (S49), fluor-buergerite (S36), lucchesiite (S47), oxy-dravite (S50), bosiite
520 (S48), and povondraite (S33). For better comparison spectra are normalized to the intensity of the ZO_6 vibration
521 and vertically offset for clarity.

522

523 **Figure 3.** Position of the ZO_6 vibration $\omega(ZO_6)$ in dependence of (a-c) the total octahedral contents of Al,
524 (Fe^{2+}+Fe^{3+}), and Mg in all samples, (d-f) the Y-site and (g-i) the Z-site contents of Al, Fe^{3+}, and Mg in all Fe^{3+}-
525 containing samples (S33, S36, S47, S48, S49, S50, S51, S57, S59). If not shown error bars are within the symbol
526 size. Data points with yellow contours refer to sample S52 for which the shown Fe^{3+} content is the sum of Fe^{3+} +
527 Mn^{3+}. Solid gray lines indicate 2nd-order polynomial fits to the corresponding sets of data points (see Table 2),
528 dashed gray lines in (h) depict the fitting functions to $\omega(ZO_6)$ vs. ^{Z}Mg [f(^{Z}Mg)] and for $\omega(ZO_6)$ vs. 6-^{Z}Al [f(6-
529 ^{Z}Al)], respectively.

530

531 **Figure 4.** (a-c) Position of the peak P3 (as labeled in Fig. 2) in dependence of the total octahedral contents of Al,
532 (Fe^{2+}+Fe^{3+}), and Mg. Symbol shape and color indicate the dominant octahedral cation. (d-f) Position of P_3 of all
533 Fe^{3+}-bearing samples in dependence of the ^{Y}Al, $^{Y}Fe^{3+}$, and ^{Y}Mg contents. Gray lines indicate linear fits of the
534 data points excluding those with yellow contours.

535

536 **Figure 5.** Intensity ratio I_1/I_2 of the two main YO_6 peaks in the range 195 to 243 cm^{-1} for all Fe^{3+}-bearing
537 samples in dependence of the Al, Fe^{3+}, and Mg content in the Y site. The gray line in (b) indicates the linear fit
538 of the data points excluding those with yellow contours. The gray line in (c) depicts a Boltzman fit $y = c_1 + (c_0 -$
539 $c_1)/(1+ \exp[(x-x_0)/dx])$.

Figure 6. Raman spectrum of the oxy-dravite showcase sample S50 in the spectral region of the framework and OH-stretching vibrations. Peak positions and selected integrated intensities are given above the peaks. Gray lines illustrate the fit functions; integrated intensities used for chemical quantification are highlighted.

This is a preprint, the final version is subject to change, of the American Mineralogist (MSA)
Cite as Authors (Year) Title. American Mineralogist, in press.
(DOI will not work until issue is live.) DOI: http://dx.doi.org/10.2138/am-2016-5820

545

Table 1. Structural formula of the studied tourmaline samples; the site populations of samples marked by * has been derived by single-crystal X-ray diffraction

#	species	general formula $XY_3Z_6(T_6O_{18})(BO_3)_3V_3W$						reference
		X	Y	Z	T	V	W	
S1	dravite	$Na_{0.79}\square_{0.12}Ca_{0.08}$	$Mg_{2.67}Al_{0.24}Fe_{0.04}Ti_{0.03}$	Al_6	Si_6	$(OH)_3$	$(OH)_{0.76}F_{0.11}O_{0.12}$	Watenphul et al. (2016)
S2	dravite	$Na_{0.76}Ca_{0.13}\square_{0.12}$	$Mg_{2.71}Al_{0.18}Fe_{0.05}Ti_{0.04}$	Al_6	$Si_{6.02}$	$(OH)_3$	$(OH)_{0.76}F_{0.13}O_{0.12}$	Watenphul et al. (2016)
S3	dravite	$Na_{0.61}\square_{0.22}Ca_{0.16}$	$Mg_{2.45}Al_{0.44}Ti_{0.05}Cr_{0.04}$	Al_6	$Si_{5.98}Al_{0.03}$	$(OH)_3$	$(OH)_{0.65}F_{0.13}O_{0.22}$	Watenphul et al. (2016)
S4	dravite	$Na_{0.65}\square_{0.22}Ca_{0.12}$	$Mg_{2.26}Al_{0.67}Ti_{0.05}$	Al_6	Si_6	$(OH)_3$	$(OH)_{0.66}F_{0.11}O_{0.23}$	Watenphul et al. (2016)
S5	dravite	$Na_{0.46}Ca_{0.39}\square_{0.13}$	$Mg_{2.65}Cr_{0.27}Ti_{0.03}$	$Al_{5.95}Cr_{0.05}$	$Si_{5.93}Al_{0.07}$	$(OH)_3$	$(OH)_{0.78}F_{0.09}O_{0.13}$	Watenphul et al. (2016)
S52	dravite	$Na_{0.68}Ca_{0.22}\square_{0.10}$	$Mg_{2.30}Fe^{2+}_{0.58}Ti_{0.12}$	$Al_{5.91}Cr_{0.07}Mg_{0.01}$	$Si_{5.95}Al_{0.05}$	$(OH)_3$	$(OH)_{0.88}O_{0.10}F_{0.02}$	this study
S53	dravite	$Na_{0.62}\square_{0.32}Ca_{0.06}$	$Mg_{2.01}Al_{0.52}Fe^{2+}_{0.41}Ti_{0.04}$	Al_6	$Si_{6.01}$	$(OH)_3$	$(OH)_{0.47}O_{0.32}F_{0.21}$	this study
S54	dravite	$Na_{0.47}Ca_{0.38}K_{0.01}\square_{0.13}$	$Mg_{1.94}Fe^{2+}_{0.91}Ti_{0.14}$	$Al_{5.94}Mg_{0.05}$	$Si_{5.89}Al_{0.11}$	$(OH)_3$	$(OH)_{0.58}F_{0.29}O_{0.13}$	this study
S55	dravite	$Na_{0.69}\square_{0.29}Ca_{0.01}$	$Mg_{1.91}Al_{0.82}Fe^{2+}_{0.20}$	Al_6	$Si_{6.05}$	$(OH)_3$	$(OH)_{0.70}O_{0.28}$	this study
S56	fluor-dravite	$Na_{0.75}\square_{0.25}$	$Mg_{1.94}Al_{0.83}Fe^{2+}_{0.14}Ti_{0.01}$	Al_6	$Si_{5.94}Al_{0.06}$	$(OH)_3$	$F_{0.42}(OH)_{0.33}O_{0.25}$	this study
S50*	oxy-dravite	$Na_{0.83}\square_{0.15}K_{0.02}$	$Al_{1.34}Mg_{1.03}Fe^{3+}_{0.58}Fe^{2+}_{0.03}Ti_{0.02}$	$Al_{4.95}Mg_{1.03}Fe^{3+}_{0.03}$	$Si_{5.98}Al_{0.02}$	$(OH)_3$	$O_{0.69}F_{0.24}(OH)_{0.07}$	Bosi and Skogby (2013)
S51*	oxy-dravite	$Na_{0.83}\square_{0.15}K_{0.02}$	$Al_{1.39}Mg_{1.11}Fe^{3+}_{0.48}Fe^{2+}_{0.02}Ti_{0.02}$	$Al_{4.90}Mg_{0.96}Fe^{3+}_{0.15}$	$Si_{5.98}Al_{0.02}$	$(OH)_3$	$O_{0.78}(OH)_{0.22}$	Bosi et al. (2016)
S57*	Fe^{3+}-rich oxy-dravite	$Na_{0.97}Ca_{0.01}K_{0.01}$	$Al_{1.01}Mg_{0.95}Mn^{3+}_{0.55}Fe^{3+}_{0.39}Ti_{0.08}Mn^{2+}_{0.02}$	$Al_{3.61}Mg_{1.35}Fe^{3+}_{1.03}$	Si_6	$(OH)_3$	$O_{0.75}(OH)_{0.22}F_{0.03}$	unpublished data
S38	uvite	$Ca_{0.41}Na_{0.39}\square_{0.21}$	$Mg_{2.54}Fe^{2+}_{0.44}Ti_{0.03}$	$Al_{5.80}Mg_{0.20}$	$Si_{5.94}Al_{0.06}$	$(OH)_3$	$(OH)_{0.69}O_{0.20}F_{0.10}$	Watenphul et al. (2016)
S39	fluor-uvite	$Ca_{0.65}Na_{0.26}\square_{0.09}$	$Mg_{2.92}Ti_{0.07}$	$Al_{5.51}Mg_{0.49}$	Si_6	$(OH)_3$	$F_{0.55}(OH)_{0.36}O_{0.09}$	Watenphul et al. (2016)
S58	fluor-uvite	$Ca_{0.61}Na_{0.36}K_{0.01}\square_{0.01}$	$Mg_{1.92}Fe^{2+}_{1.01}Ti_{0.07}$	$Al_{5.08}Mg_{0.92}$	$Si_{5.99}B_{0.01}$	$(OH)_{2.79}O_{0.21}$	$F_{0.65}(OH)_{0.23}O_{0.13}$	this study
S6	schorl	$Na_{0.64}\square_{0.30}Ca_{0.05}$	$Fe^{2+}_{1.88}Al_{0.46}Mg_{0.36}Ti_{0.03}$	Al_6	$Si_{5.93}Al_{0.07}$	$(OH)_3$	$(OH)_{0.62}O_{0.30}F_{0.07}$	Watenphul et al. (2016)
S49*	Fe^{3+}-rich schorl	$Na_{0.93}\square_{0.05}K_{0.02}$	$Fe^{3+}_{1.26}Fe^{2+}_{1.10}\square_{0.30}Al_{0.20}Ti_{0.13}Mn_{0.02}$	$Al_{5.16}Fe^{2+}_{0.53}Mg_{0.31}$	$Si_{5.88}Al_{0.12}$	$(OH)_3$	$(OH)_{0.88}O_{0.12}$	Filip et al. (2012) untreated sample

S7	fluor-schorl	$Na_{0.64}\square_{0.30}Ca_{0.05}$	$Fe^{2+}_{2.38}Al_{0.44}Mg_{0.09}Ti_{0.08}Mn_{0.02}$	Al_6	Si_6	$(OH)_3$	$F_{0.55}O_{0.23}(OH)_{0.22}$	Watenphul et al. (2016)
S8	fluor-schorl	$Na_{0.76}\square_{0.22}$	$Fe^{2+}_{2.72}Al_{0.24}Mg_{0.02}$	Al_6	$Si_{5.93}Al_{0.07}$	$(OH)_3$	$F_{0.53}(OH)_{0.25}O_{0.22}$	Watenphul et al. (2016)
S9	fluor-schorl	$Na_{0.72}\square_{0.18}Ca_{0.10}$	$Fe^{2+}_{2.58}Al_{0.61}Ti_{0.08}Mg_{0.07}Mn_{0.03}$	Al_6	Si_6	$(OH)_{2.52}O_{0.49}$	$F_{0.66}O_{0.35}$	Watenphul et al. (2016)
S10	fluor-schorl	$Na_{0.93}\square_{0.06}$	$Fe^{2+}_{1.75}Al_{0.94}Li_{0.26}Ti_{0.03}$	Al_6	Si_6	$(OH)_{2.89}O_{0.11}$	$F_{0.79}O_{0.21}$	Watenphul et al. (2016)
S44	foitite	$\square_{0.61}Na_{0.35}Ca_{0.03}$	$Fe^{2+}_{1.28}Al_{1.03}Mn_{0.41}Li_{0.18}Mg_{0.11}$	Al_6	Si_6	$(OH)_3$	$(OH)_{0.93}F_{0.07}$	Watenphul et al. (2016)
S45	foitite	$\square_{0.71}Na_{0.28}$	$Fe^{2+}_{1.52}Al_{1.04}Li_{0.29}Mn_{0.12}Mg_{0.01}$	Al_6	Si_6	$(OH)_3$	$(OH)_{0.50}O_{0.48}F_{0.02}$	Watenphul et al. (2016)
S46	□-Fe-O root name	$\square_{0.51}Na_{0.48}$	$Fe^{2+}_{1.88}Al_{0.99}Mn_{0.10}Mg_{0.01}Ti_{0.01}$	Al_6	$Si_{5.95}Al_{0.05}$	$(OH)_3$	$O_{0.51}(OH)_{0.25}F_{0.24}$	Watenphul et al. (2016)
S47*[#]	lucchesiite	$Ca_{0.69}Na_{0.30}K_{0.02}$	$Fe^{2+}_{1.44}Mg_{0.72}Al_{0.48}Ti_{0.33}V_{0.02}Mn_{0.01}Zn_{0.01}$	$Al_{4.74}Mg_{1.01}Fe^{3+}_{0.25}$	$Si_{5.85}Al_{0.15}$	$(OH)_3$	$O_{0.69}F_{0.24}(OH)_{0.07}$	Bosi et al. (2016a)
S36*	fluor-buergerite	$Na_{0.79}\square_{0.15}Ca_{0.05}$	$Fe^{3+}_{2.5}Al_{0.30}Fe^{2+}_{0.10}Ti_{0.05}Mg_{0.03}$	Al_6	$Si_{5.93}Al_{0.07}$	O_3	$F_{0.69}(OH)_{0.31}$	Watenphul et al. (2016) [a]
S59*[#]	H-rich "buergerite"	$Na_{0.93}\square_{0.05}K_{0.02}$	$Fe^{3+}_{2.00}Al_{0.40}\square_{0.30}Mg_{0.15}Ti_{0.13}Mn_{0.02}$	$Al_{4.99}Fe^{3+}_{0.87}Mg_{0.14}$	$Si_{5.90}Al_{0.10}$	$(OH)_{1.95}O_{1.05}$	$O_{0.70}(OH)_{0.30}$	Filip et al. (2012) sample A700-110h
S48*	bosiite	$Na_{0.73}Ca_{0.23}\square_{0.04}$	$Fe^{3+}_{1.47}Mg_{0.80}Fe^{2+}_{0.59}Al_{0.13}Ti_{0.02}$	$Al_{3.23}Fe^{3+}_{1.88}Mg_{0.89}$	$Si_{5.92}Al_{0.08}$	$(OH)_3$	$O_{0.85}(OH)_{0.15}$	Ertl et al. (2016)
S33*	povondraite	$Na_{0.64}K_{0.40}$	$Fe^{3+}_{2.41}Ti_{0.59}Cr_{0.02}$	$Fe^{3+}_{3.63}Mg_{1.86}Al_{0.47}$	$Si_{6.01}$	$(OH)_3$	$O_{0.96}(OH)_{0.04}$	Watenphul et al. (2016)

Notes: The total amount of boron is assigned to the B site and assumed to be 3 apfu. The occupancy disorder of Y- and Z-site cations was not studied for the samples considered by Watenphul et al. (2016) except for samples S33 and S36. The symbol □ refers to X-site vacancies. Manganese is always considered to be divalent, except for sample S57. The errors in the element contents due to chemical variations amount to 0.1 apfu in maximum.
[a] In addition to the chemistry determination by EMPA in Watenphul et al. (2016), the Fe^{2+}/Fe^{3+} ratio was determined by Mössbauer spectroscopy.
[#] annealed samples.

Table 2. Parameters of the 2nd order polynomial fits $\omega(ZO_6) = c_0 + c_1x + c_2x^2$ to the experimental data sets $\omega(ZO_6)$ versus the contents x, x = ^{Z}Al, ^{Z}Fe^{3+}, ^{Z}Mg, and and (6-^{Z}Al). The goodness of fit is given by the coefficient of determination R^2.

parameter	^{Z}Al	^{Z}Fe^{3+}	^{Z}Mg	(6–^{Z}Al)
c_0	262 ± 2	367 ± 2	375 ± 8	371 ± 1
c_1	34 ± 1	-2 ± 5	0	0
c_2	-2.5 ± 0.2	-6 ± 1	-23 ± 5	-3.1 ± 0.1
R^2	0.99	0.97	0.74	0.99
Note: c_1 for ^{Z}Fe^{3+}, ^{Z}Mg, and (6–^{Z}Al) is 0 within the uncertainties.				

This is a preprint, the final version is subject to change, of the American Mineralogist (MSA)
Cite as Authors (Year) Title. American Mineralogist, in press.
(DOI will not work until issue is live.) DOI: http://dx.doi.org/10.2138/am-2016-5820

Figure 1

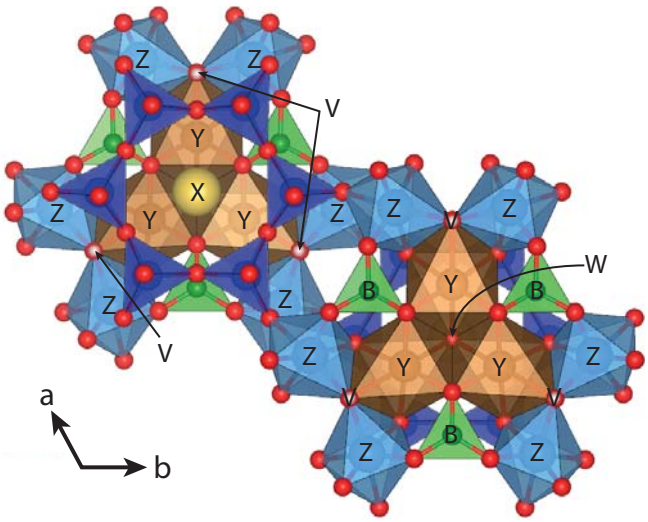

This is a preprint, the final version is subject to change, of the American Mineralogist (MSA)
Cite as Authors (Year) Title. American Mineralogist, in press.
(DOI will not work until issue is live.) DOI: http://dx.doi.org/10.2138/am-2016-5820

Figure 2

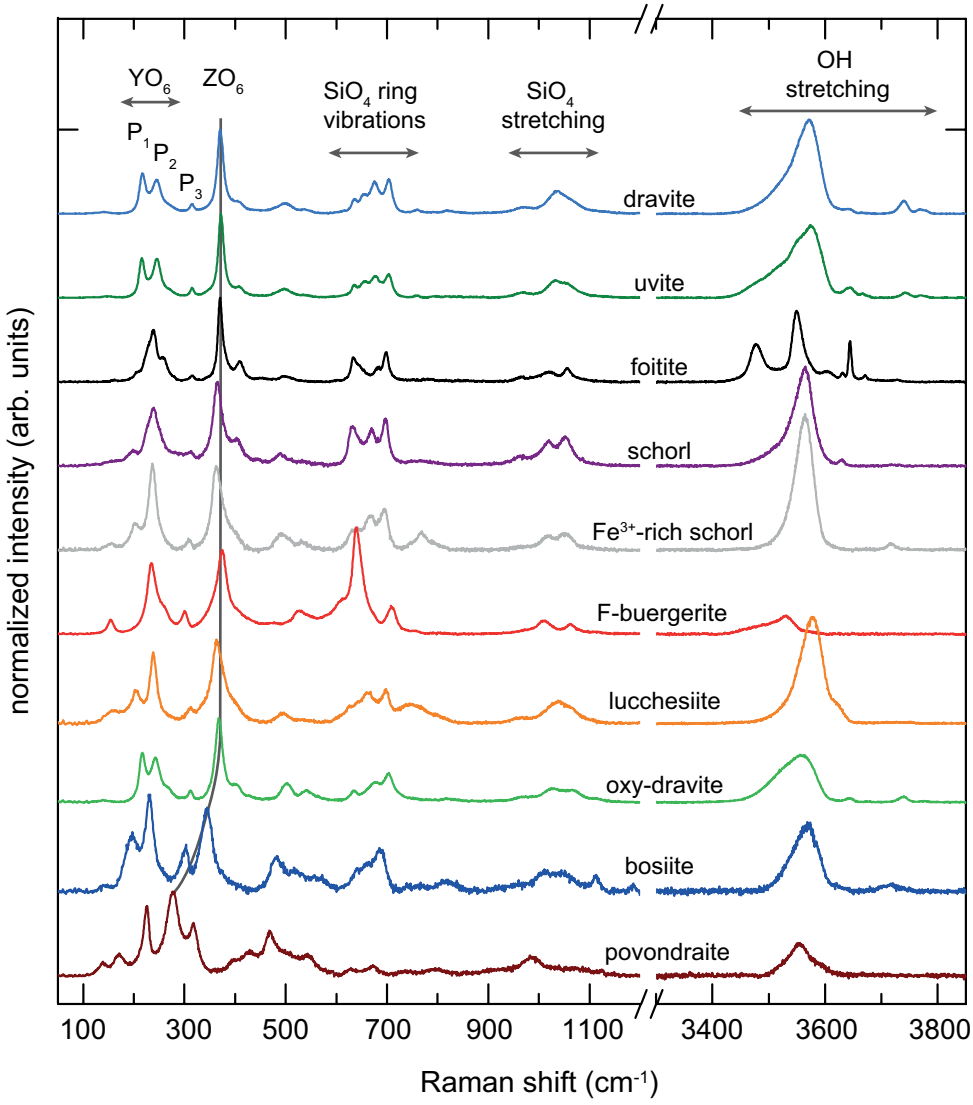

This is a preprint, the final version is subject to change, of the American Mineralogist (MSA)
Cite as Authors (Year) Title. American Mineralogist, in press.
(DOI will not work until issue is live.) DOI: http://dx.doi.org/10.2138/am-2016-5820

Figure 3

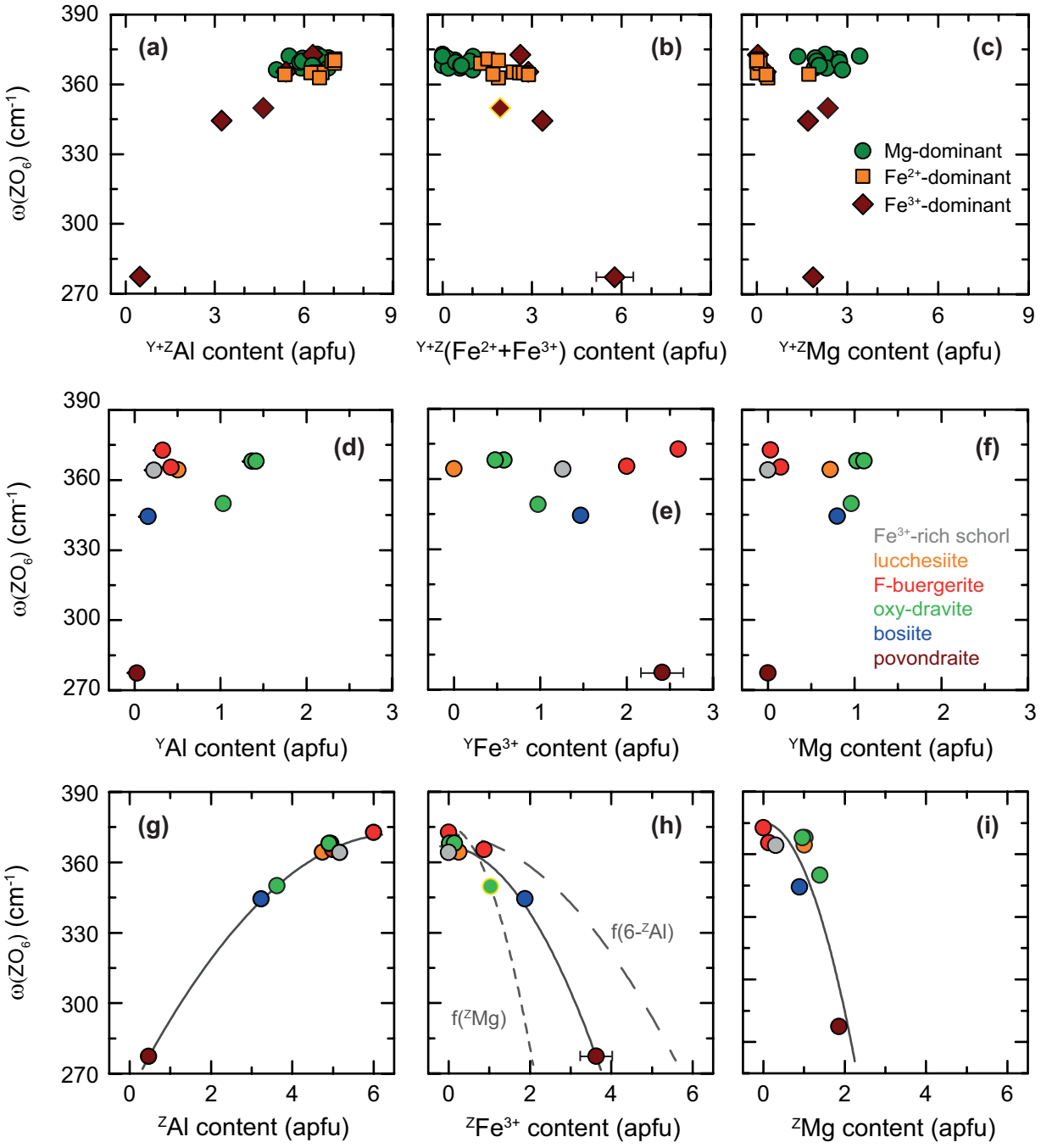

This is a preprint, the final version is subject to change, of the American Mineralogist (MSA)
Cite as Authors (Year) Title. American Mineralogist, in press.
(DOI will not work until issue is live.) DOI: http://dx.doi.org/10.2138/am-2016-5820

Figure 4

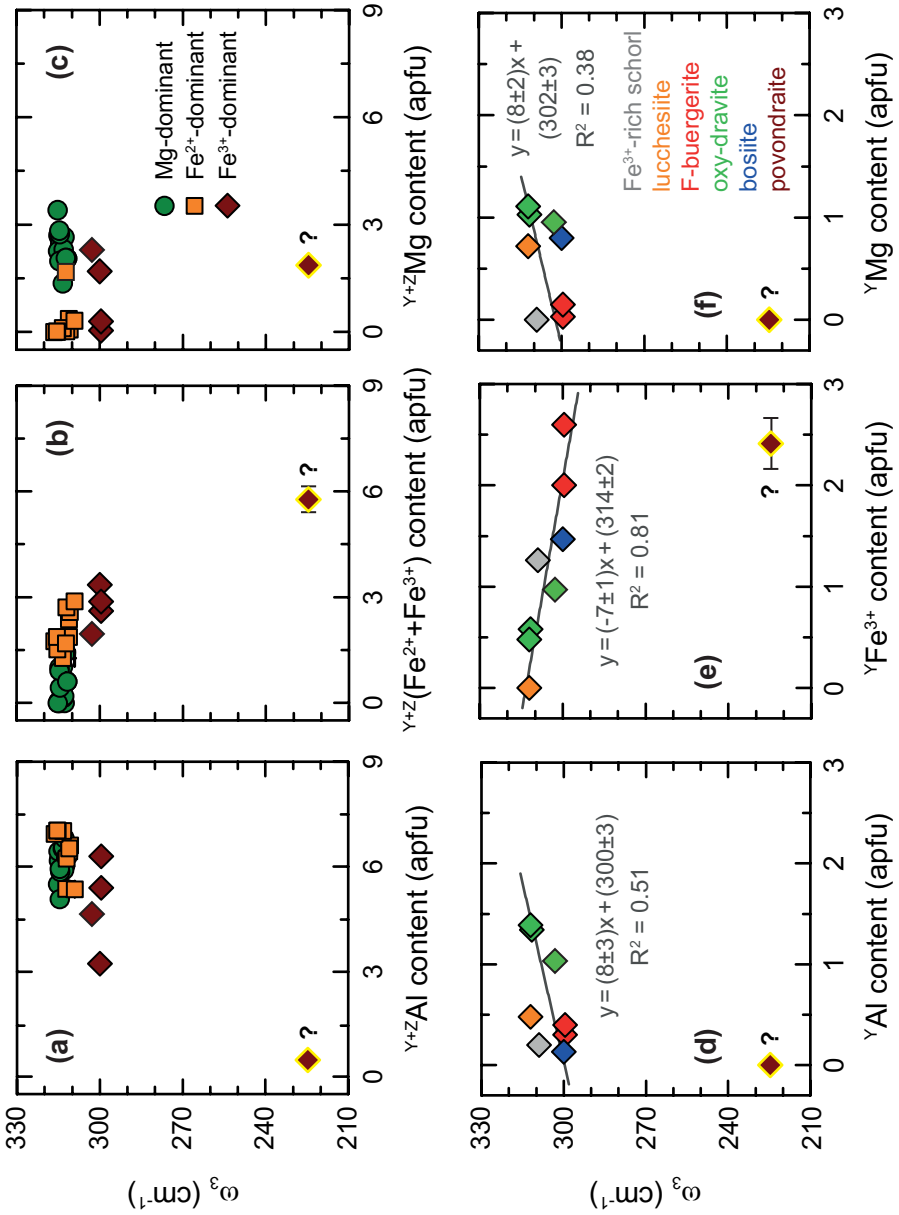

This is a preprint, the final version is subject to change, of the American Mineralogist (MSA)
Cite as Authors (Year) Title. American Mineralogist, in press.
(DOI will not work until issue is live.) DOI: http://dx.doi.org/10.2138/am-2016-5820

Figure 5

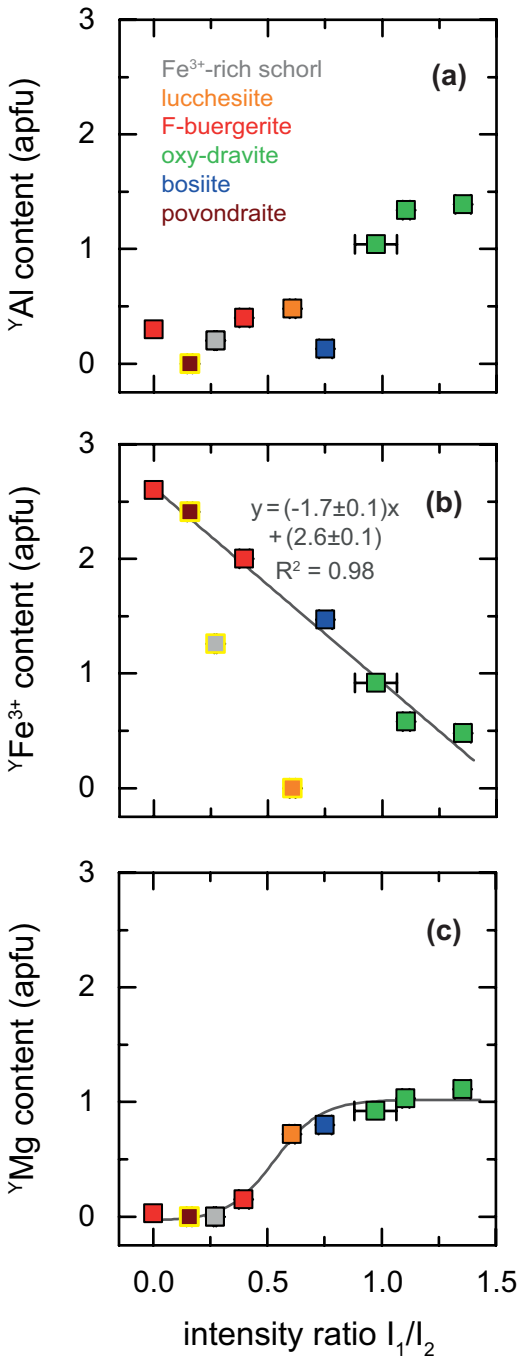

This is a preprint, the final version is subject to change, of the American Mineralogist (MSA)
Cite as Authors (Year) Title. American Mineralogist, in press.
(DOI will not work until issue is live.) DOI: http://dx.doi.org/10.2138/am-2016-5820

Figure 6